J. Fluid Mech. (2024), *vol*. 984, R1, doi:10.1017/jfm.2024.217

The propulsion direction of nanoparticles trapped in an acoustic field

Peijing Li[1], **Alexander R. Nunn**[2], **Douglas R. Brumley**[1], **John E. Sader**[3] **and Jesse F. Collis**[1],†

[1]School of Mathematics and Statistics, The University of Melbourne, Victoria 3010, Australia

[2]Department of Physics, California Institute of Technology, Pasadena, CA 91125, USA

[3]Graduate Aerospace Laboratories and Department of Applied Physics, California Institute of Technology, Pasadena, CA 91125, USA

(Received 21 December 2023; revised 5 February 2024; accepted 22 February 2024)

Solid particles trapped in an acoustic standing wave have been observed to undergo propulsion. This phenomenon has been attributed to the generation of a steady streaming flow, with a reversal in the propulsion direction at a distinct frequency. We explain the mechanism underlying this reversal by considering the canonical problem of a sphere executing oscillatory rotation in an unbounded fluid that undergoes rectilinear oscillation; these two oscillations occur at identical frequency but with an arbitrary phase difference. Two distinct bifurcations in the flow field occur: (1) a stagnation point first forms with increasing frequency, which (2) splits into a saddle node and a vortex centre. Reversal in the propulsion direction is driven by reversal in the flow far from the sphere, which coincides with the second bifurcation. This flow is identified with that of a Stokeslet whose strength is the net force exerted on the particle, which has implications for studying the flow field around particles of non-spherical geometries and for modelling suspensions of particles in acoustic fields.

Key words: propulsion, microscale transport, bifurcation

1. Introduction

A solid particle executing small-amplitude oscillations in a viscous fluid intrinsically generates a steady streaming flow. These flows have been studied extensively using both theoretical and experimental approaches with canonical problems including the rectilinear oscillation of spheres (Riley 1966; Dohara 1982; Chang & Maxey 1994; Li *et al.* 2023) and

† Email address for correspondence: jesse.collis@unimelb.edu.au

cylinders (Andres & Ingard 1953; Bertelsen, Svardal & Tjøtta 1973; Chong *et al.* 2013). Asymmetry in the particle or its motion (e.g. through shape or density) inevitably leads to an asymmetric streaming flow, which in turn can apply a steady net force on the particle, generating locomotion. This phenomenon, which is often called 'acoustic propulsion', was originally identified by Nadal & Lauga (2014) who studied the translatory oscillations of nearly spherical particles in the low-frequency limit, i.e. the particles do not perform rotational oscillations. Collis, Chakraborty & Sader (2017, 2022) subsequently studied the motion of a general asymmetric particle at arbitrary frequency, and showed that the propulsion direction reverses at a critical frequency. This finding was confirmed by Nadal & Michelin (2020) and Derr *et al.* (2022). Interestingly, Lippera *et al.* (2019) proved that to first-order in particle non-sphericity, translational oscillations alone cannot generate propulsion; contrary to Nadal & Lauga (2014). These works establish that translational and rotational particle oscillations are both required to generate propulsion. Moreover, they show that the frequency at which propulsion reverses direction is sensitively dependent on the magnitude and phase of the two oscillatory motions. The structure of streaming flows is known to change at a critical frequency (Chang & Maxey 1994; Li *et al.* 2023), indicating that this change in flow structure may somehow be connected with the change in propulsion direction. The aim of this study is to explore this connection and identify the physical mechanism giving rise to this reversal in propulsion direction. Because studies typically invoke the Lorentz reciprocal theorem to calculate the particle propulsion, an explicit calculation of the flow field, and in turn how it generates propulsion, has not been reported. We address this gap in the literature and thereby identify the physical mechanism that reverses the propulsion direction.

The steady streaming flow generated by the superposition of rectilinear and rotational motions has been investigated in several studies. Kelly (1966) studied the steady streaming flow around a cylinder undergoing coupled oscillations along and perpendicular to the cylinder's longitudinal axis. Later, Panagopoulos, Psillakis & Karahalios (1991) and Riley (1991) studied the streaming flow around a cylinder undergoing simultaneous oscillations that are rectilinearly perpendicular to and rotational around its longitudinal axis. Gopinath (1994) further studied the streaming flow around a sphere undergoing simultaneous rotational and translational oscillations, both about the same axis. Kong, Penkova & Sadhal (2017) studied a closely related problem where instead of an unbounded domain the oscillating sphere is enclosed by a larger stationary sphere. These streaming flows all exhibit an asymmetry due to the superposed motions. However, none of these works investigate whether a net force or torque arises on the solid body. It remains an open question as to how the streaming flow results in the propulsion direction reversing at a critical frequency.

Collis *et al.* (2017, 2022) and Nadal & Michelin (2020) both demonstrate that acoustic propulsion can be achieved through coupled rotation and translation of a sphere. Motivated by this observation, we study a sphere executing rotational oscillations in a viscous fluid whose far field undergoes rectilinear oscillations. This models the experimental set-up of a particle trapped at a pressure node of an acoustic field, where the particle is much smaller than the acoustic wavelength. To induce both translational and rotational oscillations, an asymmetry must be present in the sphere or its forcing, e.g. through an inhomogeneous density distribution or through the addition of magnetic fields (Valdez-Garduño *et al.* 2020). The primary focus here is to elucidate the mechanism giving rise to a reversal in propulsion direction at a critical frequency, and its connection to the generated streaming flow. In § 2 we derive an analytical solution to the flow field. In § 3 we explore the mechanism responsible for propulsion, and in particular examine bifurcations in the flow field and their connection to a reversal in the net hydrodynamic force experienced by

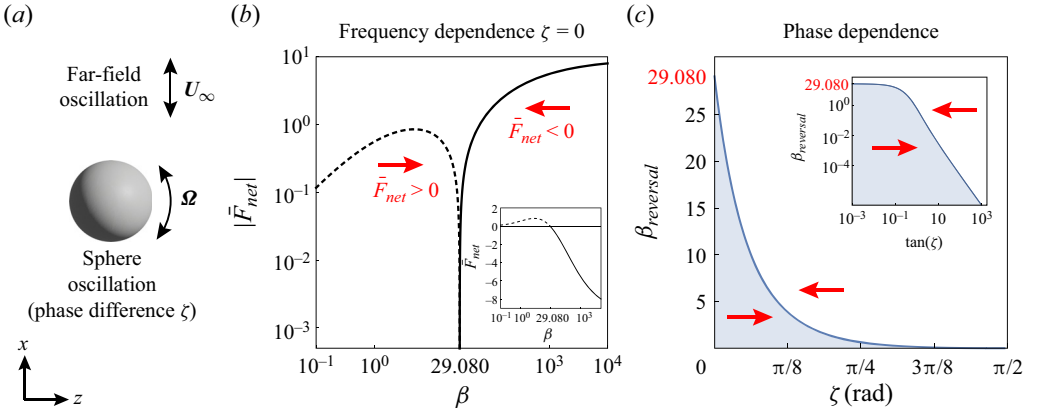

Figure 1. (*a*) Problem set-up: sphere performs small-amplitude oscillatory rotations around the *y*-axis while the far field undergoes rectilinear oscillations in the *x*-direction; the centre of the sphere is fixed so that it does not translate. (*b*) The magnitude of the net force at zero phase difference ($\zeta = 0$), scaled by the ratio of the velocity magnitudes, α, ($\bar{F}_{net} = F_{net}/\alpha$ where F_{net} is defined in (2.14)) as a function of dimensionless frequency, β. The direction of the force reverses at $\beta_{reversal} = 29.080$; dotted lines correspond to positive net force while solid lines give negative net force, in the *z*-direction. (*c*) Phase plane for the direction of the net force as a function of the phase difference, ζ. Solid blue curve is $\beta_{reversal}$. Inset plots the same function on a log–log plot but with an argument of $\tan\zeta$ to highlight the scaling behaviour as $\zeta \to \pi/2$.

the particle. Finally, in § 4 we discuss how these results may be used in modelling suspensions of acoustically propelled particles.

2. Analytical solution for the propulsion component of the streaming flow

We consider a sphere of radius R performing rotational oscillations in an unbounded, incompressible Newtonian fluid. This fluid performs independent oscillations in its far field at an identical frequency with a velocity field of $U_\infty \exp(-\mathrm{i}\omega t)\boldsymbol{i}$ where i is the imaginary unit, ω is the oscillation frequency, t is time and $\boldsymbol{i}$ is the Cartesian basis vector in the x-direction. The angular velocity of the sphere is $\Omega \exp(-\mathrm{i}(\omega t - \zeta))\boldsymbol{j}$ where $\boldsymbol{j}$ is the Cartesian basis vector in the y-direction and ζ is the phase difference between the two oscillations; see figure 1(*a*). Note that U_∞, Ω, ζ and ω are all positive and real constants with the true (as measured) quantities being given by the real parts of all expressions. Scaling the spatial variables by R, time by $1/\omega$, velocity by U_∞ and pressure by $\mu U_\infty/R$ (hence force by $\mu U_\infty R$), where μ is the fluid's shear viscosity, gives the dimensionless Navier–Stokes equations

$$\nabla \cdot \boldsymbol{u} = 0, \quad \beta\left(\frac{\partial \boldsymbol{u}}{\partial t} + \epsilon(\boldsymbol{u}\cdot\nabla)\boldsymbol{u}\right) = -\nabla p + \nabla^2 \boldsymbol{u}, \tag{2.1a,b}$$

where $\beta \equiv \rho\omega R^2/\mu$ and $\epsilon \equiv U_\infty/(\omega R)$ are the dimensionless frequency and amplitude respectively, $\boldsymbol{u}$ and p are the fluid's velocity and pressure respectively, and where ρ is the fluid's density. The dimensionless boundary conditions are

$$\boldsymbol{u}|_{|\boldsymbol{r}|=1} = \mathrm{Re}[\alpha \exp(-\mathrm{i}(t-\zeta))\boldsymbol{j}\times\boldsymbol{r}], \quad \boldsymbol{u}|_{|\boldsymbol{r}|\to\infty} = \mathrm{Re}[\mathrm{e}^{-\mathrm{i}t}\boldsymbol{i}], \tag{2.2a,b}$$

where $\boldsymbol{r}$ is the position vector from the origin and Re denotes the real part; $\alpha \equiv \Omega R/U_\infty$ is the dimensionless angular velocity around the y-axis.

The velocity and pressure fields are asymptotically expanded in the small parameter, ϵ, to give

$$\boldsymbol{u} = \mathrm{Re}[\boldsymbol{u}^{(0)}\,\mathrm{e}^{-\mathrm{i}t}] + \epsilon\boldsymbol{u}^{(1)} + o(\epsilon), \quad p = \mathrm{Re}[p^{(0)}\mathrm{e}^{-\mathrm{i}t}] + \epsilon p^{(1)} + o(\epsilon). \tag{2.3a,b}$$

This in turn ensures that the Reynolds number, $Re \equiv \epsilon\beta$, is infinitesimal for all β. The leading-order governing equations and boundary conditions are

$$\boldsymbol{\nabla}\cdot\boldsymbol{u}^{(0)} = 0, \quad -\mathrm{i}\beta\boldsymbol{u}^{(0)} = -\boldsymbol{\nabla}p^{(0)} + \nabla^2\boldsymbol{u}^{(0)}, \tag{2.4a}$$

$$\boldsymbol{u}^{(0)}|_{|\boldsymbol{r}|=1} = \alpha\,\mathrm{e}^{\mathrm{i}\zeta}\boldsymbol{j}\times\boldsymbol{r}, \quad \boldsymbol{u}^{(0)}|_{|\boldsymbol{r}|\to\infty} = \boldsymbol{i}, \tag{2.4b}$$

whose solution is readily available, e.g. Pozrikidis (1989). At $O(\epsilon)$, the governing equations and boundary conditions are

$$\boldsymbol{\nabla}\cdot\bar{\boldsymbol{u}}^{(1)} = 0, \quad \frac{\beta}{4}((\boldsymbol{u}^{(0)}\cdot\boldsymbol{\nabla})\boldsymbol{u}^{(0)*} + (\boldsymbol{u}^{(0)*}\cdot\boldsymbol{\nabla})\boldsymbol{u}^{(0)}) = -\boldsymbol{\nabla}\bar{p}^{(1)} + \nabla^2\bar{\boldsymbol{u}}^{(1)}, \tag{2.5a}$$

$$\bar{\boldsymbol{u}}^{(1)}|_{|r|=1} = \boldsymbol{0}, \quad \bar{\boldsymbol{u}}^{(1)}|_{|r|\to\infty} = \boldsymbol{0}, \tag{2.5b}$$

where $\bar{\boldsymbol{u}}^{(1)}$ and $\bar{p}^{(1)}$ are the steady components of $\boldsymbol{u}^{(1)}$ and $\boldsymbol{p}^{(1)}$ respectively, and the * denotes the complex conjugate. Note that the $O(\epsilon)$ flow also has a component at twice the frequency of the leading-order flow, which does not contribute to the streaming flow. To obtain the cycle-averaged pathlines, $\bar{\boldsymbol{u}}_p^{(1)}$, from the first-order velocity field, the Stokes drift velocity (Longuet-Higgins 1953)

$$\bar{\boldsymbol{u}}_p^{(1)} = \bar{\boldsymbol{u}}^{(1)} + \frac{\mathrm{i}}{4}((\boldsymbol{u}^{(0)}\cdot\boldsymbol{\nabla})\boldsymbol{u}^{(0)*} - (\boldsymbol{u}^{(0)*}\cdot\boldsymbol{\nabla})\boldsymbol{u}^{(0)}) \tag{2.6}$$

is included.

The $O(\epsilon)$ solution (reported here for the first time) is calculated by performing a general expansion in spherical harmonics,

$$\bar{p}^{(1)} = \sum_{l=0}^{\infty}\sum_{m=-l}^{l}\bar{p}_{l,m}^{(1)}(r)Y_{l,m}, \tag{2.7a}$$

$$\bar{\boldsymbol{u}}^{(1)} = \sum_{l=0}^{\infty}\sum_{m=-l}^{l}(\bar{u}_{l,m}^{(1)}(r)\boldsymbol{Y}_{l,m} + \bar{v}_{l,m}^{(1)}(r)\boldsymbol{\Psi}_{l,m} + \bar{w}_{l,m}^{(1)}(r)\boldsymbol{\Phi}_{l,m}), \tag{2.7b}$$

where the scalar spherical harmonics, $Y_{l,m}$, and vector spherical harmonics, $\boldsymbol{Y}_{l,m}$, $\boldsymbol{\Psi}_{l,m}$ and $\boldsymbol{\Phi}_{l,m}$, follow the same notations and definitions as Barrera, Estevez & Giraldo (1985); r is the spherical radial coordinate and the spherical harmonics are functions of the polar, θ, and azimuthal, ϕ angles. The radial functions, i.e. those that depend on r, are calculated by substituting (2.7*a*) and (2.7*b*), along with the leading-order solution from (2.4*a*), into (2.5*a*). Using the orthogonality of spherical harmonics, and the linearity of (2.5*a*) in $\bar{\boldsymbol{u}}^{(1)}$ and $\bar{p}^{(1)}$, we obtain an inhomogeneous ordinary differential equation in r for each (l, m) pair. Each ordinary differential equation may then be easily solved using a Green's function.

2.1. *Streaming flow components that give rise to a net force*

By symmetry, the net force on the particle is in the z-direction, which upon substitution of (2.7) into the definition of the force gives

$$\boldsymbol{F} = 4\sqrt{\frac{\pi}{3}}\left(\bar{u}^{(1)}_{1,0}(1) - \bar{v}^{(1)}_{1,0}(1) + \frac{\mathrm{d}}{\mathrm{d}r}(\bar{u}^{(1)}_{1,0} + \bar{v}^{(1)}_{1,0})|_{r=1} - \frac{1}{2}\bar{p}^{(1)}_{1,0}(1)\right)\boldsymbol{k}, \tag{2.8}$$

where $\boldsymbol{k}$ is the Cartesian basis vector in the z-direction. Equation (2.8) reveals that only the $l = 1, m = 0$ components of the velocity field (2.7*b*) contribute to the net force. We denote this component of the flow the 'net-force flow', whose solution is

$$p^{(1)}_{net} = \sqrt{\frac{\pi}{3}}\bar{p}^{(1)}_{1,0}(r)Y_{1,0}, \tag{2.9a}$$

$$\boldsymbol{u}^{(1)}_{net} = \sqrt{\frac{\pi}{3}}(\bar{u}^{(1)}_{1,0}(r)\boldsymbol{Y}_{1,0} + \bar{v}^{(1)}_{1,0}(r)\boldsymbol{\Psi}_{1,0}), \tag{2.9b}$$

where

$$\bar{u}^{(1)}_{1,0}(r) = \frac{F_{net}}{r} + 2\alpha\mathrm{Re}\left(K_1(r) + K_2(r) - \frac{K_1(1) + K_2(1)}{r^3}\right) + 2\alpha\mathrm{Re}\left(Q_1(r) + Q_2(r) - \frac{Q_1(1) + Q_2(1)}{r^3}\right), \tag{2.10a}$$

$$\bar{v}^{(1)}_{1,0}(r) = \bar{u}^{(1)}_{1,0}(r) + \frac{r}{2}\frac{\partial\bar{u}^{(1)}_{1,0}(r)}{\partial r}, \tag{2.10b}$$

$$\bar{p}^{(1)}_{1,0}(r) = \frac{F_{net}}{r^2} + 2\alpha\mathrm{Re}(L_1(r) + L_2(r) + L_3(r) + L_4(r)), \tag{2.10c}$$

and

$$K_1(r) = \frac{\exp\left(\dfrac{(1-\mathrm{i})\sqrt{\beta}}{\sqrt{2}} + \mathrm{i}\zeta\right)((3+3\mathrm{i}) + 3\mathrm{i}\sqrt{2\beta} - (1-\mathrm{i})\beta)(\beta^3 r^2 - 10\mathrm{i}\beta^2)}{960(\sqrt{2\beta} + (1-\mathrm{i}))} \times E_1\left(\frac{(1-\mathrm{i})\sqrt{\beta}r}{\sqrt{2}}\right), \tag{2.11a}$$

$$K_2(r) = -\frac{\exp(\sqrt{2\beta} + \mathrm{i}\zeta)(2 + (1+\mathrm{i})\sqrt{2\beta})(\beta^3 r^2 + 5\mathrm{i}\beta^2)}{80(\beta + \sqrt{2\beta} + 1)}E_1(\sqrt{2\beta}r), \tag{2.11b}$$

$$Q_1(r) = -\frac{\exp\left(-\dfrac{(1-\mathrm{i})\sqrt{\beta}(r-1) + \mathrm{i}\zeta}{\sqrt{2}}\right)}{960(\sqrt{2\beta} + (1+\mathrm{i}))r^4}\left(480r(\sqrt{2\beta}r + (1+\mathrm{i})) + \left(\frac{1}{2} + \frac{\mathrm{i}}{2}\right) \times ((1+\mathrm{i})\beta + 3\sqrt{2\beta} + (3-3\mathrm{i}))((4\mathrm{i}-4)\beta r^2 - 4\sqrt{2\beta}r + (60+60\mathrm{i}) - 8\mathrm{i}\sqrt{2}\beta^{3/2}r^3 + \sqrt{2}\beta^{5/2}r^5 - (1+\mathrm{i})\beta^2 r^4)\right), \tag{2.12a}$$

$$Q_2(r) = \frac{(1+\mathrm{i})\sqrt{2}\exp(-\sqrt{2\beta}(r-1) + \mathrm{i}\zeta)}{160(\sqrt{2\beta} + (1+\mathrm{i}))r^4}(-((3+5\mathrm{i})\sqrt{2}\beta r^2) + (12+10\mathrm{i})\sqrt{\beta}r + 15\mathrm{i}\sqrt{2} + (2+10\mathrm{i})\beta^{3/2}r^3 + 2\beta^{5/2}r^5 - \sqrt{2}\beta^2 r^4), \tag{2.12b}$$

$$L_1(r) = \frac{\exp\left(\frac{(1-\mathrm{i})\sqrt{\beta}}{\sqrt{2}}\right)((3+3\mathrm{i}) + 3\mathrm{i}\sqrt{2\beta} - (1-\mathrm{i})\beta)\beta^3 r}{96(\sqrt{2\beta} + (1+\mathrm{i}))} E_1\left(\frac{(1-\mathrm{i})\sqrt{\beta}}{\sqrt{2}} r\right), \tag{2.13a}$$

$$L_2(r) = -\frac{(1-\mathrm{i})\exp(\sqrt{2\beta} + \mathrm{i}\zeta)(\mathrm{i}\sqrt{2\beta} + (1+\mathrm{i}))\beta^3 r}{8(\beta + \sqrt{2\beta} + 1)} E_1(\sqrt{2\beta} r), \tag{2.13b}$$

$$\begin{aligned} L_3(r) = &-\frac{\sqrt{2}\exp\left(-\frac{(1-\mathrm{i})(r-1)\sqrt{\beta}}{\sqrt{2}} + \mathrm{i}\zeta\right)}{192(\sqrt{2\beta} + (1+\mathrm{i}))r^5}((1+\mathrm{i})\beta + 3\sqrt{2\beta} + (3-3\mathrm{i})) \\ &\times (6\mathrm{i}\sqrt{2}\beta r^2 + (24-24\mathrm{i})\sqrt{\beta} r + 24\sqrt{2} \\ &- (2+2\mathrm{i})\beta^{3/2} r^3 - (1-\mathrm{i})\beta^{5/2} r^5 + \sqrt{2}\beta^2 r^4), \end{aligned} \tag{2.13c}$$

$$\begin{aligned} L_4(r) = &\frac{\sqrt{2}\exp(-\sqrt{2\beta}(r-1) + \mathrm{i}\zeta)}{16(\beta + \sqrt{2\beta} + 1)r^5}(3\sqrt{2}\beta r((1-2\mathrm{i})r + (2-2\mathrm{i})) \\ &+ \sqrt{\beta}((6-6\mathrm{i}) - 12\mathrm{i}r) - 6\mathrm{i}\sqrt{2} + \beta^{3/2}(2r^3 + (9-3\mathrm{i})r^2) \\ &+ \sqrt{2}\beta^2((1+\mathrm{i}) - r)r^3 + \beta^{5/2}(2r^5 - (1+\mathrm{i})r^4) + (1+\mathrm{i})\sqrt{2}\beta^3 r^5). \end{aligned} \tag{2.13d}$$

The net force (in the z-direction) has the explicit form

$$F_{net} = \alpha(\mathrm{e}^{\mathrm{i}\zeta} g(\beta) + \mathrm{e}^{-\mathrm{i}\zeta} g^*(\beta)), \tag{2.14}$$

where

$$\begin{aligned} g(\beta) = &\frac{\beta}{768(1 + \sqrt{2\beta} + \beta)}\left(48\sqrt{2}\mathrm{i} + (144 + 48\mathrm{i})\sqrt{\beta} + (51 - 72\mathrm{i})\sqrt{2}\beta\right. \\ &- (25 + 13\mathrm{i})\beta^{3/2} + (2 + 8\mathrm{i})\sqrt{2}\beta^2 - (5 - 3\mathrm{i})\beta^{5/2} + \sqrt{2}\mathrm{i}\beta^3 \\ &+ \exp\left(\frac{(1+\mathrm{i})\sqrt{\beta}}{\sqrt{2}}\right) E_1\left(\frac{(1+\mathrm{i})\sqrt{\beta}}{\sqrt{2}}\right)\beta(6\mathrm{i} + \beta)((1-\mathrm{i})\beta^{3/2} \\ &+ 4\sqrt{2}\beta + (6 + 6\mathrm{i})\sqrt{\beta} + 3\mathrm{i}\sqrt{2}) \\ &\left.-24\mathrm{i}\,\mathrm{e}^{\sqrt{2\beta}} E_1(\sqrt{2\beta})\beta(3\mathrm{i} - \beta)(\sqrt{2} + (1-\mathrm{i})\sqrt{\beta})\right), \end{aligned} \tag{2.15}$$

and $E_1(z) \equiv \int_1^\infty \tau^{-1}\,\mathrm{e}^{-z\tau}\,\mathrm{d}\tau$ is the exponential integral function. Equations (2.10)–(2.15) are given in a supplementary Mathematica notebook available at https://doi.org/10.1017/jfm.2024.217 to assist the reader in their implementation. While (2.14) and (2.15) are identical to the result obtained using the Lorentz reciprocal theorem as required (Collis *et al.* 2022), we now have a solution for the flow field driving propulsion.

3. Mechanism for the reversal in propulsion direction

Expressing (2.14) in dimensional form reveals that the force is proportional to $U_\infty \Omega$, with these quantities not appearing elsewhere, i.e. the net force, F_{net}, is quadratic in amplitude, as expected. Because U_∞ and Ω are positive real constants, (2.14) further reveals that

the reversal in propulsion can only depend on the dimensionless frequency, β, and the phase difference, ζ. We first examine the case where $\zeta = 0$, i.e. the rectilinear and angular velocities are in phase. Figure 1(*b*) shows the magnitude of F_{net}/α, i.e. F_{net} but with the dimensionless angular velocity, α, scaled out. The reversal in propulsion occurs at $\beta_{reversal} = 29.080$; note that all numericised quantities are reported to five significant figures. As $\beta \to 0$, we find $F_{net} \to 0$ and as $\beta \to \infty$, F_{net} approaches a constant. This trend is true regardless of the value of ζ. Figure 1(*c*) shows how the reversal frequency varies as ζ is increased from zero: it is maximal when the rectilinear and angular velocities are directly in phase, and monotonically decreases with increasing phase difference, approaching zero when $\zeta = \pi/2$.

3.1. *Topological structure of the net-force flow*

We now examine the cycle-averaged pathlines, which we henceforth refer to as pathlines; the streamlines and pathlines differ by the Stokes drift velocity, see (2.6). In the low-frequency regime, $\beta \ll 1$, Stokes drift contributes significantly to the pathlines. However, at frequencies near and above $\beta_{reversal}$, which we are primarily interested in here, the Stokes drift velocity is small. The Stokes drift velocity decays exponentially as a function of distance from the particle, r, and does not contribute to the flow in the far field.

We now analyse in detail the case where the two motions are in phase, $\zeta = 0$; other phase differences show similar trends but at reduced frequencies; figure 1(*c*). Figure 2(*a–f*) shows the pathlines of the net-force flow (2.9*b*), in the z–x plane at $y = 0$, at dimensionless frequencies $\beta = 10, 16.817, 25, 29.080, 35, 50$; note that this flow is axisymmetric about the z-axis. These values of β are chosen to highlight typical flow fields at, above and below the two bifurcations.

Two distinct bifurcations occur at different values of β; the first bifurcation occurs at $\beta = 16.817$, and the second coincides with $\beta_{reversal} = 29.080$. At frequencies below the first bifurcation, all cycle-averaged pathlines move in the negative z-direction; figure 2(*a*). At the first bifurcation, a stagnation point forms at a radius of $r = 2.1736$; figure 2(*b*). As β increases, the stagnation point then splits into a saddle node and a vortex centre; see figure 2(*c*). As β continues to increase, the vortex centre moves towards the sphere while the saddle node moves away from the sphere. The saddle node continues to move away from the sphere until it vanishes at $\beta_{reversal} = 29.080$, at which point the vortex encompasses the entire domain, i.e. all pathlines are closed. The pathlines exhibit a similar structure to a source dipole, decaying at a rate of $1/r^3$, and results in $F_{net} = 0$; figure 2(*d*). As β increases above $\beta_{reversal}$, a boundary emerges, which separates an inner vortex from an outer region. In the asymptotic limit as $\beta \to \infty$, the outer flow becomes independent of β, aligning with calculations of different streaming flows in this limit, e.g. Riley (1966). The pathlines in this outer region move in the opposite direction to those in the outer region for $\beta < \beta_{reversal}$. As we shall show in § 3.2, this drives the change in direction of F_{net}. See Bhosale, Parthasarathy & Gazzola (2020) and Chan *et al.* (2022) for further discussion on the bifurcations that occur in related viscous streaming flows.

3.2. *Connection between F_{net} and the far-field flow*

The exact solution for the steady streaming flow, (2.9), has the form of a multipole expansion. We therefore obtain the flow in the far field by keeping only the slowest decaying terms as $r \to \infty$. This shows that far from the particle, the flow is that of a

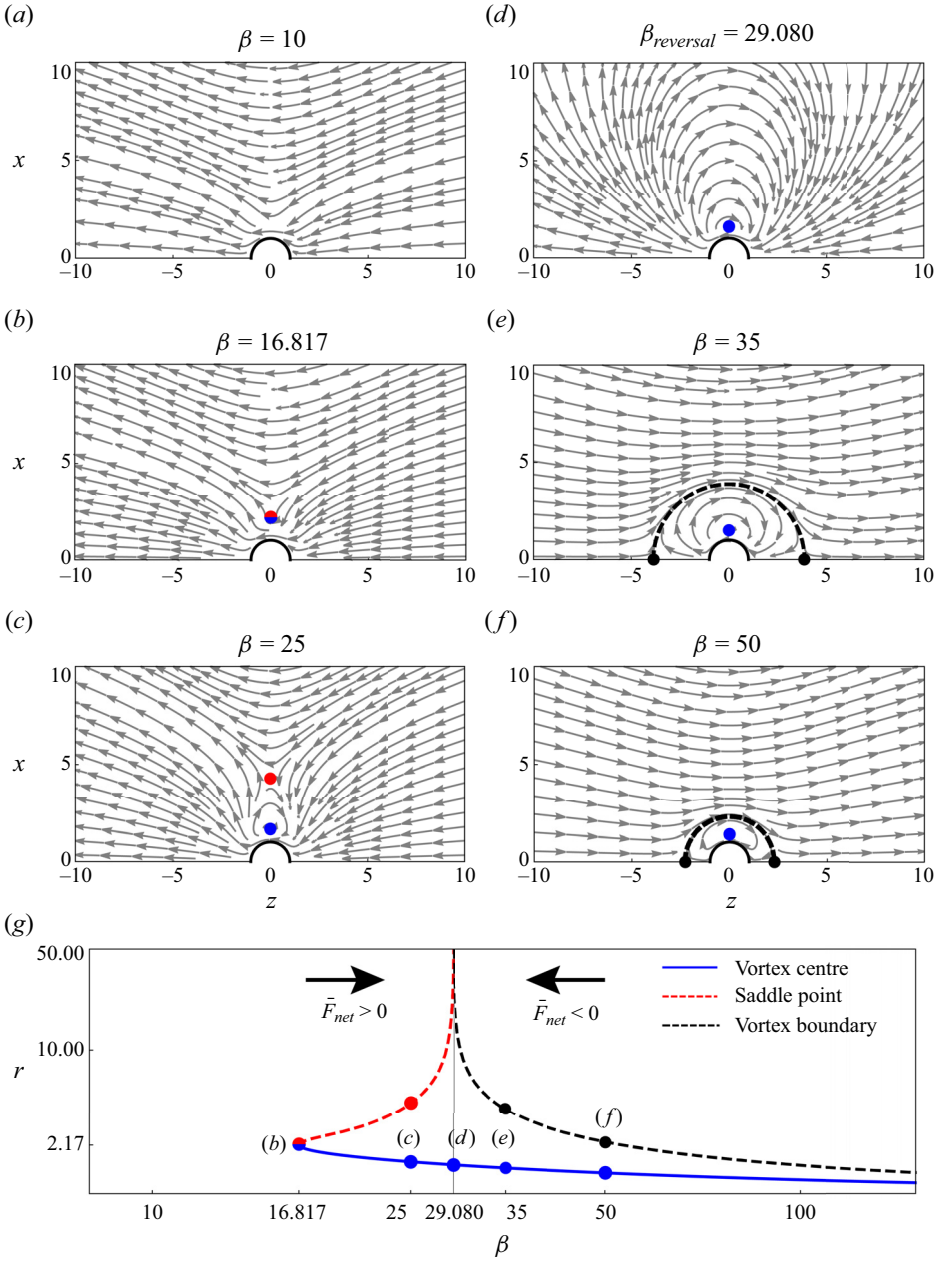

Figure 2. (*a–f*) Cycle-averaged pathlines at values of β selected to illustrate the different regimes. Pathlines are plotted in the z–x plane but are axisymmetric about the z-axis. The stagnation points of the flow are given by dots. (*g*) Bifurcation diagram of β vs the r values (spherical radial coordinate) where the stagnation points occur. Dots coincide with those reported in (*a–f*). All results correspond to $\zeta = 0$.

Stokeslet with strength F_{net}:

$$\bar{p}^{(1)} \sim -\frac{\boldsymbol{r}}{4\pi|\boldsymbol{r}|^3} \cdot F_{net}\boldsymbol{k}, \quad |\boldsymbol{r}| \to \infty, \tag{3.1a}$$

$$\bar{\boldsymbol{u}}^{(1)} \sim -\frac{1}{8\pi}\left(\frac{\boldsymbol{I}}{|\boldsymbol{r}|} + \frac{\boldsymbol{rr}}{|\boldsymbol{r}|^3}\right) \cdot F_{net}\boldsymbol{k}, \quad |\boldsymbol{r}| \to \infty, \tag{3.1b}$$

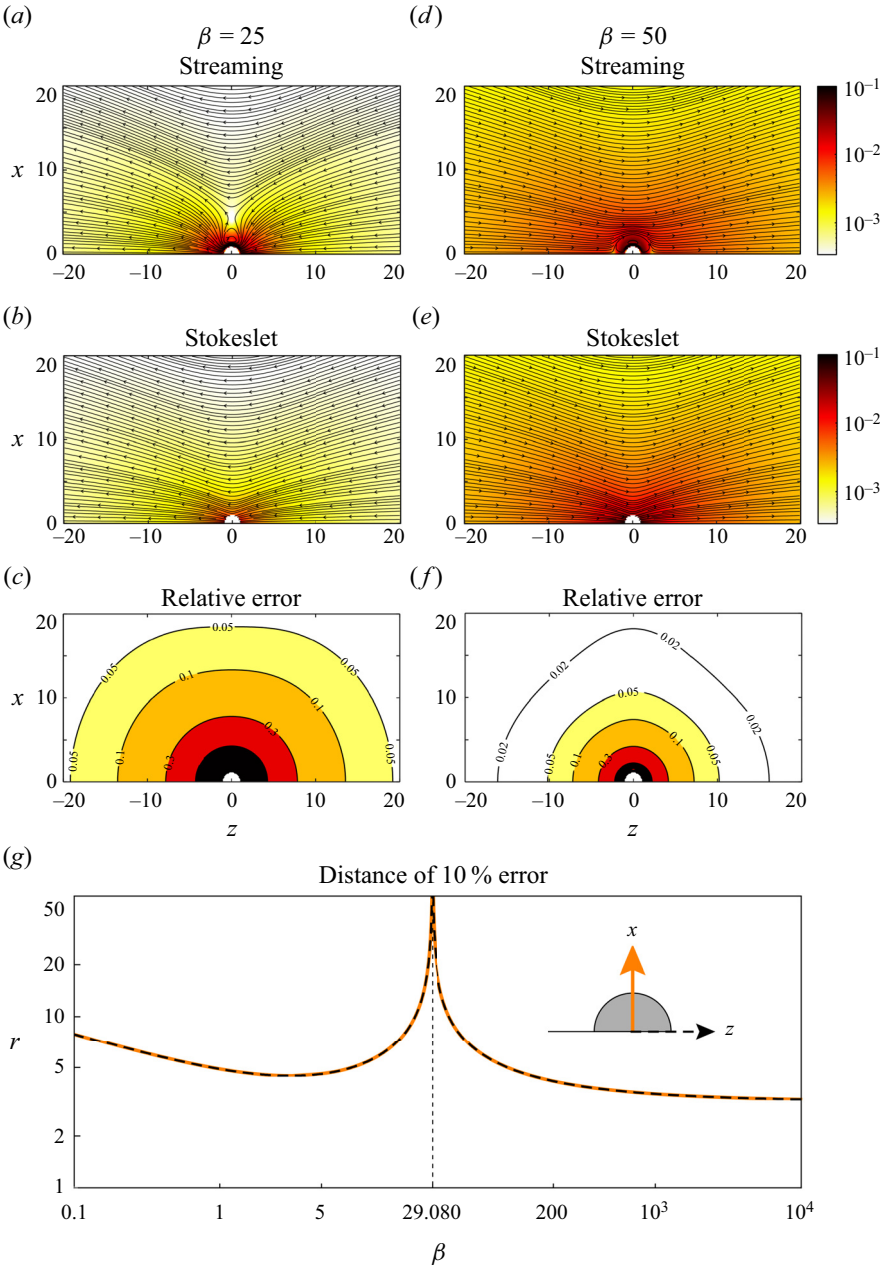

Figure 3. (*a–f*) Net-force flow (pathlines), equivalent Stokeslet (pathlines) and relative error between the two flows for $\beta = 25$ and $\beta = 50$; $\zeta = 0$ in both cases. The colour bar gives the flow magnitude with the dimensionless angular velocity, α, scaled out. (*g*) Minimum bound on the (spherical) radial distance, r, from the origin where the error is 10 % or less.

where $\boldsymbol{I}$ is the identity tensor and F_{net} is defined in (2.14). Note that the oscillatory disturbances, and components of the steady flow that do not lead to a net force, have velocity fields which decay faster than $1/r$. This establishes that the bifurcation that switches the direction of the far-field pathlines switches the direction of the Stokeslet which is connected to F_{net} by (3.1).

4. Discussion and conclusions

We have investigated the origin of the reversal in the direction of acoustically propelled nanoparticles by examining a model problem of a sphere performing oscillatory rotations in a rectilinearly oscillating velocity field. This sheds light on the flow field that drives acoustic propulsion which is yet to be reported; the Lorentz reciprocal theorem is usually used instead. This revealed two distinct bifurcations that result in a change to the direction of the pathlines in the far field at a critical value of the dimensionless frequency, which directly leads to the reversal in the net hydrodynamic force on the particle.

This connection between the far-field pathlines and the net force was facilitated by showing the far-field flow exactly corresponds to an equivalent Stokeslet. The equivalent Stokeslet representation of the far-field streaming flow is not unique to solid particles with spherical geometries. Using the boundary integral formulation of Stokes flows and performing a multipole expansion, it can be shown that the leading-order multipole is always a Stokeslet; this is due to the fast decay of the body force in (2.5*a*). The strength of the Stokeslet, however, will in general not be given by F_{net} for non-spherical bodies; this is because the net force will in general include effects due to the Lagrangian motion of the particle, e.g. Collis *et al.* (2022).

Given many acoustic propulsion experiments use suspensions of particles (Wang *et al.* 2012; Ahmed *et al.* 2014), it is of interest to investigate at what distance the flow can be replaced by its equivalent Stokeslet. This could alleviate the need to calculate the complex nature of the flow field in the vicinity of each particle when performing computational simulations of these suspensions. Figure 3(*a–f*) gives the streaming flow, equivalent Stokeslet, and relative difference between these flows for $\beta = 25$ and $\beta = 50$, which are below and above $\beta_{reversal} = 29.080$, respectively. As expected, the difference vanishes as $r \to \infty$; figure 3(*c*,*f*). Figure 3(*g*) shows the minimum radial distance from the sphere where the difference is 10 % or less. When $\beta \to \beta_{reversal}$, this difference diverges as the net force vanishes and there is no equivalent Stokeslet at the reversal frequency. As the flow field at $\beta_{reversal}$ resembles a source dipole in the particle's far field, inclusion of this multipole may improve the overall accuracy of the singularity representation of the flow field. Acoustically propelled particles are confined to a two-dimensional plane, i.e. the pressure node, and thus suspensions of such particles provide an intriguing set-up for investigating collective dynamics. Considering these suspensions as a superposition of singularity solutions, confined to lie in a monolayer, provides direct access to the vast array of literature on collective dynamics in Stokes flows (Elgeti, Winkler & Gompper 2015), including applications such as tracer diffusion in suspensions of active particles (Leptos *et al.* 2009) and phase behaviour and rheology of dense active colloids (Ishikawa, Brumley & Pedley 2021).

Supplementary material. Supplementary material is available at https://doi.org/10.1017/jfm.2024.217.

Funding. The authors acknowledge the support of the Melbourne Research Scholarship.

Declaration of interests. The authors report no conflict of interest.

Author ORCIDs.
Peijing Li https://orcid.org/0009-0009-0459-4460;
Alexander R. Nunn https://orcid.org/0009-0007-6977-8741;
Douglas R. Brumley https://orcid.org/0000-0003-0587-0251;
John E. Sader https://orcid.org/0000-0002-7096-0627;
Jesse F. Collis https://orcid.org/0000-0003-0992-101X.

References

Ahmed, S., Gentekos, D.T., Fink, C.A. & Mallouk, T.E. 2014 Self-assembly of nanorod motors into geometrically regular multimers and their propulsion by ultrasound. *ACS Nano* **8** (11), 11053–11060.

Andres, J.M. & Ingard, U. 1953 Acoustic streaming at low Reynolds numbers. *J. Acoust. Soc. Am.* **25** (5), 932–938.

Barrera, R.G., Estevez, G.A. & Giraldo, J. 1985 Vector spherical harmonics and their application to magnetostatics. *Eur. J. Phys.* **6** (4), 287–294.

Bertelsen, A., Svardal, A. & Tjøtta, S. 1973 Nonlinear streaming effects associated with oscillating cylinders. *J. Fluid Mech.* **59** (3), 493–511.

Bhosale, Y., Parthasarathy, T. & Gazzola, M. 2020 Shape curvature effects in viscous streaming. *J. Fluid Mech.* **898**, A13.

Chan, F.K., Bhosale, Y., Parthasarathy, T. & Gazzola, M. 2022 Three-dimensional geometry and topology effects in viscous streaming. *J. Fluid Mech.* **933**, A53.

Chang, E.J. & Maxey, M.R. 1994 Unsteady flow about a sphere at low to moderate Reynolds number. Part 1. Oscillatory motion. *J. Fluid Mech.* **277**, 347–379.

Chong, K., Kelly, S.D., Smith, S. & Eldredge, J.D. 2013 Inertial particle trapping in viscous streaming. *Phys. Fluids* **25**, 033602.

Collis, J.F., Chakraborty, D. & Sader, J.E. 2017 Autonomous propulsion of nanorods trapped in an acoustic field. *J. Fluid Mech.* **825**, 29–48.

Collis, J.F., Chakraborty, D. & Sader, J.E. 2022 Autonomous propulsion of nanorods trapped in an acoustic field–corrigendum. *J. Fluid Mech.* **935**, E1.

Derr, N.J., Dombrowski, T., Rycroft, C.H. & Klotsa, D. 2022 Reciprocal swimming at intermediate Reynolds number. *J. Fluid Mech.* **952**, A8.

Dohara, N. 1982 The unsteady flow around an oscillating sphere in a viscous fluid. *J. Phys. Soc. Japan* **51** (12), 4095–4103.

Elgeti, J., Winkler, R.G. & Gompper, G. 2015 Physics of microswimmers—single particle motion and collective behavior: a review. *Rep. Prog. Phys.* **78** (5), 056601.

Gopinath, A. 1994 Steady streaming due to small-amplitude superposed oscillations of a sphere in a viscous fluid. *Q. J. Mech. Appl. Maths* **47** (3), 461–480.

Ishikawa, T., Brumley, D.R. & Pedley, T.J. 2021 Rheology of a concentrated suspension of spherical squirmers: monolayer in simple shear flow. *J. Fluid Mech.* **914**, A26.

Kelly, R.E. 1966 Streaming effects associated with doubly oscillating cylinders. *Q. J. Mech. Appl. Maths* **19** (4), 473–484.

Kong, D., Penkova, A. & Sadhal, S.S. 2017 Oscillatory and streaming flow between two spheres due to combined oscillations. *J. Fluid Mech.* **826**, 335–362.

Leptos, K.C., Guasto, J.S., Gollub, J.P., Pesci, A.I. & Goldstein, R.E. 2009 Dynamics of enhanced tracer diffusion in suspensions of swimming eukaryotic microorganisms. *Phys. Rev. Lett.* **103** (19), 198103.

Li, P., Collis, J.F., Brumley, D.R., Schneiders, L. & Sader, J.E. 2023 Structure of the streaming flow generated by a sphere in a fluid undergoing rectilinear oscillation. *J. Fluid Mech.* **974**, A37.

Lippera, K., Dauchot, O., Michelin, S. & Benzaquen, M. 2019 No net motion for oscillating near-spheres at low Reynolds numbers. *J. Fluid Mech.* **866**, R1.

Longuet-Higgins, M.S. 1953 Mass transport in water waves. *Phil. Trans. R. Soc. Lond.* A **245** (903), 535–581.

Nadal, F. & Lauga, E. 2014 Asymmetric steady streaming as a mechanism for acoustic propulsion of rigid bodies. *Phys. Fluids* **26**, 082001.

Nadal, F. & Michelin, S. 2020 Acoustic propulsion of a small, bottom-heavy sphere. *J. Fluid Mech.* **898**, A10.

Panagopoulos, A.A., Psillakis, Z.M. & Karahalios, G.T. 1991 Steady streaming induced by a cylinder performing transverse and torsional oscillations. *Phys. Fluids* A **3** (5), 782–792.

Pozrikidis, C. 1989 A singularity method for unsteady linearized flow. *Phys. Fluids* A **1** (9), 1508–1520.

Riley, N. 1966 On a sphere oscillating in a viscous fluid. *Q. J. Mech. Appl. Maths* **19** (4), 461–472.

Riley, N. 1991 Oscillating viscous flows. II. Superposed oscillations. *Mathematika* **38**, 203–216.

Valdez-Garduño, M., Leal-Estrada, M., Oliveros-Mata, E.S., Sandoval-Bojorquez, D.I., Soto, F., Wang, J. & Garcia-Gradilla, V. 2020 Density asymmetry driven propulsion of ultrasound-powered janus micromotors. *Adv. Funct. Mater.* **30** (50), 2004043.

Wang, W., Castro, L.A., Hoyos, M. & Mallouk, T.E. 2012 Autonomous motion of metallic microrods propelled by ultrasound. *ACS Nano* **6** (7), 6122–6132.